

# Inertial migration and axial control of deformable capsules<sup>†</sup>

Christian Schaaf<sup>\*a</sup> and Holger Stark<sup>a</sup>

Received Xth XXXXXXXXXX 20XX, Accepted Xth XXXXXXXXXX 20XX

First published on the web Xth XXXXXXXXXX 200X

DOI: 10.1039/b000000x

The mechanical deformability of single cells is an important indicator for various diseases such as cancer, blood diseases and inflammation. Lab-on-a-chip devices allow to separate such cells from healthy cells using hydrodynamic forces. We perform hydrodynamic simulations based on the lattice-Boltzmann method and study the behavior of an elastic capsule in a microfluidic channel flow in the inertial regime. While inertial lift forces drive the capsule away from the channel center, its deformability favors migration in the opposite direction. Balancing both migration mechanisms, a deformable capsule assembles at a specific equilibrium distance depending on its size and deformability. We find that this equilibrium distance is nearly independent of the channel Reynolds number and falls on a single master curve when plotted versus the Laplace number. We identify a similar master curve for varying particle radius. In contrast, the actual deformation of a capsule strongly depends on the Reynolds number. The lift-force profiles behave in a similar manner as those for rigid particles. Using the Saffman effect, the capsule's equilibrium position can be controlled by an external force along the channel axis. While rigid particles move to the center when slowed down, very soft capsules show the opposite behavior. Interestingly, for a specific control force particles are focused on the same equilibrium position independent of their deformability.

## 1 Introduction

The mechanical deformability of biological cells is a sensitive quantity for identifying various diseases<sup>1</sup>. Tumor cells, for example, are much softer than healthy cells<sup>2,3</sup>, while malaria-infected red blood cells become much stiffer when occupied by the parasite<sup>4,5</sup>. Microfluidic lab-on-a-chip devices utilize hydrodynamic effects in order to separate and probe biological cell samples<sup>6–9</sup>. Such lab-on-a-chip devices are easy to use and can be designed as mass product. They are thus a helpful tool for especially improving medical conditions in poor countries<sup>10</sup>.

The dynamics of deformable particles such as vesicles<sup>11</sup>, capsules<sup>12,13</sup>, or red blood cells<sup>14,15</sup> has mostly been studied at low Reynolds numbers. Deformable particles migrate towards regions of low shear gradient. Thus, when immersed in a Poiseuille flow they move towards the channel center<sup>16</sup>.

At medium Reynolds numbers Segré and Silberberg observed that rigid particles in Poiseuille flow assemble in an annulus roughly half way between the center and the wall of a channel with circular cross section<sup>17,18</sup>. Thus, in the non-uniform flow profile an inertial lift force occurs that initiates a drift motion directed away from the channel center. At the equilibrium distance this force is compensated by repulsive particle-wall interaction. The Segré-Silberberg effect is well studied in experiments<sup>19–21</sup>, in theory using matched asymptotics<sup>22,23</sup>, and in simulations<sup>24,25</sup>. While the original setup

used a cylindrical channel, microfluidic experiments are usually conducted with quadratic or rectangular channels, as they are easier to manufacture. Due to the reduced symmetry, the circular annulus is replaced by eight off-centered equilibrium positions in case of a quadratic channel (four on the main axes and four on the diagonals) or two on the short axes of a rectangular channel<sup>26,27</sup>.

In recent years also the dynamics of deformable particles in the inertial regime has been studied<sup>28–33</sup>. In particular, Hur *et al.*<sup>34</sup> demonstrated with their experiments that particles can be separated from each other based on their elastic deformability. Indeed, particles move closer to the channel center the softer and also the larger they are. This effect was also studied in simulations<sup>35,36</sup>. Although all results agree that soft particles move to the channel center, the influence of the Reynolds number is not completely clear. While in some cases the final equilibrium distance from the channel center seems to depend on the Reynolds number<sup>37,38</sup>, Kilimnik *et al.*<sup>35</sup> found no evidence of such a behavior in their computer simulations. In contrast, they showed that the recorded values of the equilibrium distance collapse on a single master curve when plotted against the deformability of the particles.

Using additional control forces along the channel axis allows for further adjustment of the particles' equilibrium positions. In their experiments Kim and Yoo<sup>39</sup> demonstrated that particles can be focused by applying an axial control force. They used an electric field to slow down the particles relative to the fluid. Due to the induced Saffman force, the particles migrated towards the channel center<sup>40</sup>. While these ex-

<sup>a</sup> Institute of Theoretical Physics, Technical University Berlin, Hardenbergstr. 36, 10623 Berlin, Germany; E-mail: Christian.Schaaf@tu-berlin.de

periments were performed at small Reynolds numbers, previous simulation work at moderate Reynolds numbers<sup>27</sup> showed how an axial control force can move a rigid particle against the inertial lift force to a new equilibrium position. This position sensitively depends on the strength of the control force and the particle radius. Finally, the inertial focusing of particles can also be influenced by controlling their rotational motion<sup>41</sup> or by designing external force fields with the help of optimal control theory<sup>42</sup>.

In this article we study the dynamics of a single deformable elastic capsule flowing through a microchannel with quadratic cross section. To simulate the Newtonian fluid, we employ the lattice-Boltzmann method together with the immersed boundary method. In the first part we study in detail the equilibrium positions of the elastic capsules, their deformations in the inertial Poiseuille flow, as well as the scaling of the lift-force profile by varying Reynolds number, particle rigidity, and radius. In an intermediate regime of particle rigidity, we confirm that the equilibrium distance hardly depends on Reynolds number and also identify a similar master curve for varying particle radius. The lift-force profiles behave in a similar manner as those for rigid particles.

In the second part we apply an external axial force to allow for an additional control of the equilibrium position. Extending the study of rigid particles in Ref.<sup>27</sup>, we find that a speed-up of the particle first induces a drift further away from the channel center, which then reverses for even stronger speed-up. This effect becomes more pronounced as the particles are softer. For very soft particles the behavior is opposite to rigid particles. A strong speed-up pushes them to the channel center while they move away from the center when slowed down. Interestingly, for a specific external control force all particles assemble at the same equilibrium distance independent of their deformability.

The article is organized as follows. In sect. 2 we explain the set-up of our system, some details of the lattice-Boltzmann method, how we model deformable capsules, and the measurement of the lift-force profiles. In sect. 3 we present the results including the detailed study of the equilibrium position, the deformations of the capsules, the lift-force profiles, and finally the influence of an external control force. We summarize and close with final remarks in sect. 4.

## 2 Methods

### 2.1 Microfluidic setup in the simulations

We study a single deformable elastic capsule flowing in a microfluidic channel with a quadratic cross section (edge length  $2w$  and channel length  $L$ ; see Fig. 1). The pressure-driven Poiseuille flow points along the  $z$  direction and the origin of the coordinate system is in the channel center. The channel

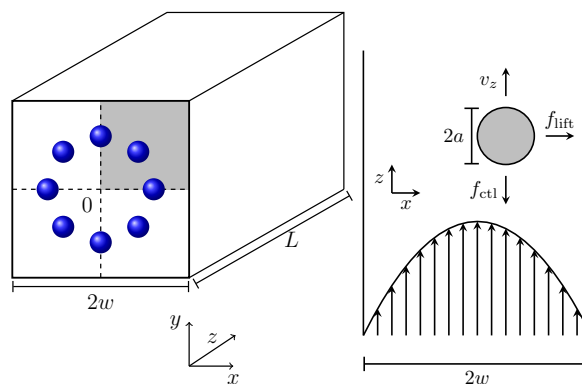


**Fig. 1** Left: Schematic of the microfluidic setup in the simulations. We use a quadratic channel with edge length  $2w$  and channel length  $L$ . The channel center is located at  $x, y = 0$ . Due to the symmetry of the quadratic cross section, only the shaded area needs to be considered. The blue spheres indicate possible stable equilibrium positions. Right: Poiseuille flow in the  $xz$  plane. The undeformed capsule with radius  $a$ , lift ( $f_{\text{lift}}$ ) and control ( $f_{\text{ctl}}$ ) forces acting on it, and the axial capsule velocity  $v_z$  are indicated.

is filled with a Newtonian fluid with density  $\rho$  and kinematic viscosity  $\nu$ . A constant local body force (see sect. 2.2) generates the almost parabolic Poiseuille flow of a square channel<sup>43</sup>. It is characterized by the channel Reynolds number  $\text{Re} = 2wu_{\text{max}}/\nu$ , where  $u_{\text{max}}$  is the maximal flow velocity in the channel center.

Inside the channel we place a deformable, neutrally buoyant particle, which is filled with a fluid with the same viscosity as the surrounding medium. We model the deformable capsule by the Skalak model and characterize its deformability by the Laplace number (see sect. 2.3). In such a setup the capsule shows cross-streamline migration within the cross section due to three effects: i) Already at zero Reynolds number deformable capsules migrate towards the channel center, where shear rate vanishes, even in unbounded parabolic flow<sup>16</sup>. This effect is important for the Fåhræus-effect<sup>44</sup>. ii) At non-vanishing Reynolds number the parabolic flow profile generates a dynamic pressure difference along the particle surface. Thereby an inertial lift force occurs that drives the particle outwards towards the channel walls as indicated in Fig. 1<sup>45</sup>. iii) Finally, a wall-induced lift force acts against the inertial lift force<sup>46</sup>. All three effects ultimately determine the equilibrium position of the particle in the channel cross section.

The time for migrating towards the equilibrium position depends on the fluid parameters. Typically, in our simulations the particles assembled at their final location after 10 to 100  $w^2/\nu$ . With a channel width of  $50\mu\text{m}$  and the kinematic viscosity of water,  $1 \times 10^{-6} \text{ m}^2/\text{s}$ , this corresponds to  $2.5 \times 10^{-2} \text{ s}$  to  $0.25 \text{ s}$ . Our longest simulations are equivalent

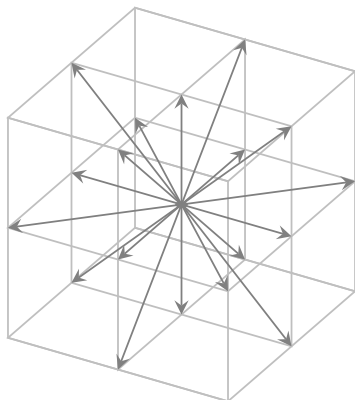


**Fig. 2** Set of velocity vectors for the D3Q19 implementation of the LBM. Six vectors point to the center of the faces, 12 to the center of the edges, and one is the zero velocity.

to 1 s.

In addition, an external control force applied on the capsule along the channel axis can tune this equilibrium position. For example, when directed against the flow (see Fig. 1), the positive control force  $\vec{f}_{\text{ctrl}}$  slows down the particle. Thereby, the relative velocity between particle surface and surrounding fluid changes. This modifies the dynamic pressure difference along the particle surface and a lateral migration known as Saffman effect occurs<sup>40</sup>.

## 2.2 Lattice-Boltzmann method

The viscous fluid is simulated by the lattice-Boltzmann method (LBM) in 3D with 19 different velocity vectors (D3Q19) using the Bhatnagar-Gross-Krook (BGK) collision model<sup>47,48</sup>. The LBM generates a solution of the Navier-Stokes equations by solving the Boltzmann equation on a cubic lattice. For this the one-particle distribution function  $f(\vec{x}, \vec{v}, t)$  for position  $\vec{x}$  and velocity  $\vec{v}$  is discretized in space on a cubic lattice and for a discrete set of velocity vectors. These vectors point to the center of the faces and edges of a cube (Fig. 2). The time evolution of the Boltzmann equation is governed by two alternating steps:

$$\text{collision: } f_i^*(\vec{x}, t) = f_i(\vec{x}, t) + \frac{1}{\tau} [f_i^{\text{eq}}(\vec{x}, t) - f_i(\vec{x}, t)] \quad (1)$$

$$\text{streaming: } f_i(\vec{x} + \vec{c}_i \Delta t, t + \Delta t) = f_i^*(\vec{x}, t), \quad (2)$$

where  $f_i(\vec{x}, t)$  is the discretized particle distribution function with the index  $i$  indicating the velocity vectors,  $f_i^{\text{eq}}$  is an expansion of the Maxwell-Boltzmann distribution up to second order in the mean velocity, and  $\tau$  is a typical relaxation time from the BGK model.

Macroscopic quantities like the density  $\rho$  or the momentum density  $\rho \vec{u}$  correspond to the first two moments of the distribution function with respect to velocity:

$$\rho(\vec{x}, t) = \sum_i f_i(\vec{x}, t) \quad (3)$$

$$\rho(\vec{x}, t) \vec{u}(\vec{x}, t) = \sum_i \vec{c}_i f_i(\vec{x}, t). \quad (4)$$

Following the Chapman-Enskog theory<sup>49</sup>, one can derive a relation between the relaxation time  $\tau$  and the fluid viscosity  $\nu$ ,

$$\nu = c_s^2 \Delta t \left( \tau - \frac{1}{2} \right), \quad (5)$$

where  $c_s^2 = \frac{1}{3}$  is the speed of sound measured in LBM units. It is important to note that the LBM is only valid for small Mach numbers  $\text{Ma} = u_{\text{max}}/c_s$  to ensure the incompressibility of the Newtonian fluid. We chose the maximum flow velocity such that  $\text{Ma} \leq 0.1$  for all our simulations, which corresponds to density variations of less than 1%.

Simulations with immersed-boundaries like our deformable capsules show the best accuracy for relaxation times  $\tau \leq 1$  or viscosities  $\nu \leq 1/6$ , according to Eq. (5) with LBM time step  $\Delta t = 1$ . We tuned  $\text{Re}$  by varying  $\nu$  through  $\tau$  for Mach number  $\text{Ma} = 0.1$ . When  $\tau = 1$  was reached, we fixed this time and  $\nu = 1/6$  and lowered  $\text{Ma}$  to obtain the desired Reynolds numbers  $\text{Re} < 50$ .

To simulate the pressure-driven Poiseuille flow, we implemented a constant body force  $\vec{g}$  following the Guo force scheme<sup>50</sup>. In this scheme the fluid momentum density at each time step is modified according to

$$\rho \vec{u} = \sum_i c_i f_i + \frac{\Delta t}{2} \vec{g}. \quad (6)$$

As lattice-Boltzmann solver we used the code provided by the Palabos project<sup>51</sup>. The deformable capsule was implemented with the help of the immersed-boundary method as described in the following section.

Our simulations were conducted with a length-to-width ratio of  $L/2w = 4$  using periodic boundary conditions along the channel ( $z$ -axis). As resolution for the lattice-Boltzmann solver, we chose 120 cubic unit cells along the full width of the channel, when we recorded trajectories of the capsules, and 90 cells for determining the lift-force profiles. Especially for soft particles ( $\text{La} = 1$  to 10) and high Reynolds numbers ( $\text{Re} = 100$ ) the lift force was not constant but oscillating in time. To avoid these oscillations, the resolution was enhanced to 180 cells.

## 2.3 Modeling a deformable capsule

To couple the deformable capsule to the fluid, we use the immersed-boundary method<sup>52–54</sup>. In this method the capsule is modeled with a deformable Lagrangean grid, which moves

in the fixed Eulerian grid of the LBM. The Lagrangean mesh of the undeformed spherical capsule is obtained by starting from an icosahedron and then repeatedly subdividing each triangle into four triangles such that the distance between two neighboring vertices is approximately equal to the lattice spacing of the Eulerian grid. The membrane forces are calculated on the Lagrangean mesh and interpolated to the grid of the fluid. Likewise, the velocities of the mesh vertices are determined by an interpolation from the fluid velocity vectors of the surrounding grid nodes. For both interpolations a weighting function  $\phi(r)$  is used, which averages over all lattice nodes within a distance  $\Delta x$  from the center, where  $\Delta x$  is 2. For further details we refer to<sup>54</sup>.

To model the capsule, three contributions need to be considered: in-plane elasticity of the capsule membrane, its bending stiffness, and volume conservation due to the incompressible fluid interior. Elastic deformations are described by the Skalak model, which originally was introduced for red blood cells<sup>55</sup>. The elastic energy is written in the strain invariants  $I_1$  and  $I_2$  of the Green strain tensor as defined in appendix A.2,

$$E_s = \int_{A_0} dA \left[ \frac{\kappa_s}{12} (I_1^2 + 2I_1 - 2I_2) + \frac{\kappa_a}{12} I_2^2 \right], \quad (7)$$

where  $\kappa_s$  is the shear modulus governing shear deformations and  $\kappa_a$  is the area modulus, which penalizes changes in the area of the mesh triangles relative to the initial value.

Bending stiffness is needed to prevent buckling of the capsules and the formation of cusps. To quantify bending elasticity, we take the Helfrich functional, which can be discretized on the triangular surface mesh<sup>56,57</sup>,

$$E_b = \sqrt{3} \kappa_b \sum_{\langle ij \rangle} [1 - \cos(\theta_{ij} - \theta_{ij}^{(0)})] \quad (8)$$

where  $\kappa_b$  is the bending modulus,  $\theta_{ij}$  is the angle between the normal vectors of two neighboring triangles, and  $\theta_{ij}^{(0)}$  is the reference angle for the spherical capsule. Finally, to approximately ensure volume conservation, we added an energy of the form

$$E_v = \frac{\kappa_v}{2} \frac{(V - V^{(0)})^2}{V^{(0)}}, \quad (9)$$

where  $\kappa_v$  is the elastic bulk modulus,  $V$  the volume of the capsule, and  $V^{(0)}$  the volume of the spherical ground state. We chose  $\kappa_v$  such that the volume changes were less than 1%. To reduce the number of variable parameters, we followed Krüger *et al.*<sup>37</sup> and fixed the ratios of the area and the bending moduli with the shear modulus,

$$\kappa_a / \kappa_s = 2 \quad \kappa_b / (\kappa_s a^2) = 2.87 \times 10^{-3}. \quad (10)$$

The capillary number  $Ca$ , as the ratio between applied viscous shear stress  $\rho v u_{\max} / w$  and typical elastic stress

$\kappa_s / a$ , describes the deformability of an elastic capsule,

$$Ca = \frac{\rho v u_{\max} a}{w \kappa_s}. \quad (11)$$

The capillary number still depends on the explicit flow speed. A dimensionless number to quantify the rigidity of a capsule is the Laplace number. It is defined as the ratio between typical elastic shear forces  $\kappa_s a$  and the intrinsic viscous force scale  $\rho v^2$ . Using the particle Reynolds number  $Re_p = Re(a/w)^2$ , one can write the Laplace number as

$$La = \frac{Re_p}{Ca} = \frac{\kappa_s a}{\rho v^2} \quad (12)$$

We will see that it is the right quantity to plot the equilibrium distance of a capsule from the channel center.

## 2.4 Measurement of the lift-force profile

To determine the inertial lift force acting on the capsule, we fix its lateral position and measure the force of the LB fluid on the membrane following<sup>41</sup>. To hold the capsule in place, we apply an adjustable force  $f_{\text{fb}}$  evenly distributed over all the membrane vertices, which compensates the lift force. To calculate this feedback force, we use a proportional-integral (PI) feedback controller<sup>58</sup>. The idea is to steer a system parameter, here the lateral position, by an external force  $f_{\text{fb}}$  in a targeted state. In our case the dynamics of the lateral position of the capsule's center of mass,  $\vec{x}_{\text{com}}$ , is determined by

$$\dot{\vec{x}}_{\text{com}} = \vec{f}_{\text{lift}} + \vec{f}_{\text{fb}}. \quad (13)$$

The feedback force depends on the deviation of the control parameter from the desired state at the current and all previous times,

$$\vec{f}_{\text{fb}}(t) = \gamma_x [\vec{x}_0 - \vec{x}_{\text{com}}(t)] + \int_0^t \gamma_u [\vec{x}_0 - \vec{x}_{\text{com}}(t')] dt', \quad (14)$$

where  $\gamma_{u/x}$  are the stiffnesses of the feedback controller and  $\vec{x}_0$  is the targeted lateral position. In steady state,  $\dot{\vec{x}}_{\text{com}} = 0$ , one obtains  $\vec{f}_{\text{lift}} = -\vec{f}_{\text{fb}}$ . The lift force is averaged over at least 200000 time steps, where the first 20000 time steps, until the system equilibrates, are neglected.

## 3 Results

### 3.1 Equilibrium position

We first study in detail the equilibrium position of one single capsule varying particle radius  $a$ , its deformability measured by the capillary number  $Ca$  or the Laplace number  $La$ , and the channel Reynolds number  $Re$ . We vary the Laplace number in

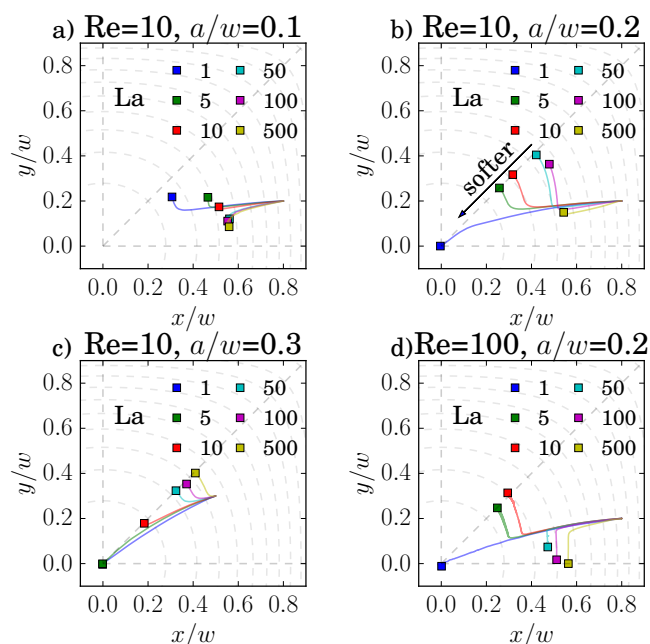


**Fig. 3** Trajectories of the capsules in the cross-sectional plane of the channel with different rigidities quantified by the Laplace number  $La$ . The trajectories are plotted for different particle sizes  $a/w$  and Reynolds numbers  $Re$  as indicated in a)-d). The capsules start at the same position and the endpoint of the trajectories are shown by filled squares. Not all of them reach their equilibrium position on the diagonal or the main axis during the simulations.

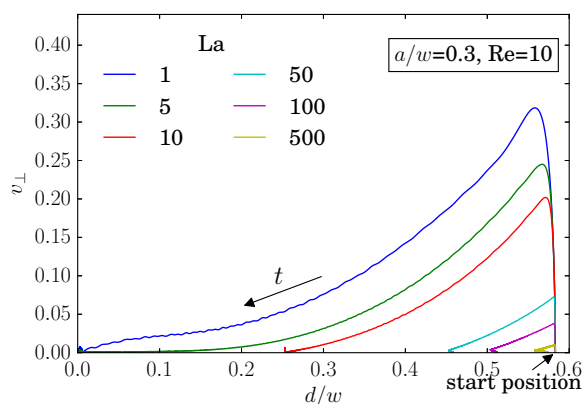


**Fig. 4** Lateral velocity  $v_{\perp}$  plotted versus the distance  $d$  to the channel center for different Laplace numbers  $La$ . All particles start at the same initial position ( $d/w = 0.583$ ) and with time move inwards to their equilibrium positions.

the interval between 1 (very soft) and 1000 (almost rigid) or the capillary number between  $10^{-4}$  and 10. For the Reynolds number we choose the values 5, 10, 50 and 100.

We used two different methods to determine the equilibrium position of the capsule. The first method is closer to the experiment. The particle is put at a specific position and can then move freely. Figure 3 shows a collection of example trajectories. Especially the small particles with  $a/w = 0.1$  at  $Re = 10$  migrate slowly and do not reach their equilibrium positions on either the diagonal or the  $x$  axis, even in the longest simulation runs. The reason is that the lift force driving the particle motion strongly scales with particle radius  $a$  and Reynolds number, as discussed in sect. 3.3 but also depends on the deformability of the capsule. However, in most cases one clearly sees where the particles migrate to.

For the particle trajectories, which we visualize in Fig. 3c), we plot in Fig. 4 the lateral velocity  $v_{\perp}$  in the cross-sectional plane of the channel versus the distance  $d$  from the center. All particles start at the same position at a distance  $d/w = 0.583$ . The velocity rapidly increases and then gradually decreases to zero as the particles move inwards towards their equilibrium position. Clearly, softer particles (small  $La$ ) show a larger lateral migration velocity than rigid particles. For the smaller particles in Fig. 3b) the migration process itself splits into two phases. First, the particles quickly move inwards along the radial direction. This corresponds to the gradual decrease of the lateral velocity as discussed in Fig. 4. When the capsules are close to their final equilibrium distance, the radial movement stops and the lateral velocity is close to zero. Thus, the particles only very slowly drift along the polar direction towards their equilibrium positions. A similar kind of motion was already observed for rigid particles<sup>24</sup>.

To have a computationally more efficient method for determining the equilibrium positions, we also measured lift-force profiles using the method outlined in sect. 2.4. The equilibrium positions correspond to the stable fix points. We will discuss the lift-force profiles in more detail in sect. 3.3. Both methods agree well, as we demonstrate in Fig. A1 in appendix A.1. For the following discussion based on Fig. 5 we will take the equilibrium positions determined from the lift-force profiles. The free migration of the capsules indicate that they mostly lie on the diagonals. Only small capsules ( $a/w = 0.1$ ) and capsules at  $Re = 100$ , which are sufficiently rigid ( $La > 50$ ), clearly migrate towards the  $x$  axis. The results on the rigid particles are in agreement with our earlier work<sup>27</sup>.

We now discuss the equilibrium distance from the channel center,  $d_{eq}$ , in more detail. In the inset of Fig. 5a) we plot it versus the deformability of the capsule, the capillary number  $Ca$ , for different Reynolds numbers  $Re$ . All curves show how deformable capsules (large  $Ca$ ) migrate to the channel center. Making them more rigid by decreasing  $Ca$ , the inertial lift force becomes more dominant and drives the cap-

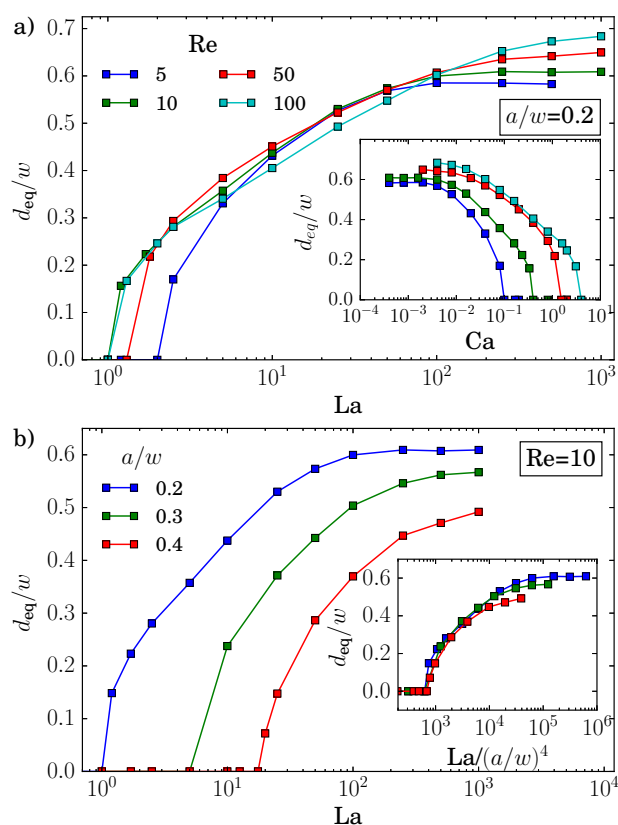


**Fig. 5** Equilibrium distance  $d_{eq}/w$  from the channel center: a) plotted versus Laplace number  $La$  for  $a/w = 0.2$  and different  $Re$ , Inset:  $d_{eq}/w$  versus capillary number  $Ca$ ; b)  $d_{eq}/w$  plotted versus  $La$  for  $Re = 10$  and different  $a/w$ , Inset:  $d_{eq}/w$  versus  $La/(a/w)^4$ .

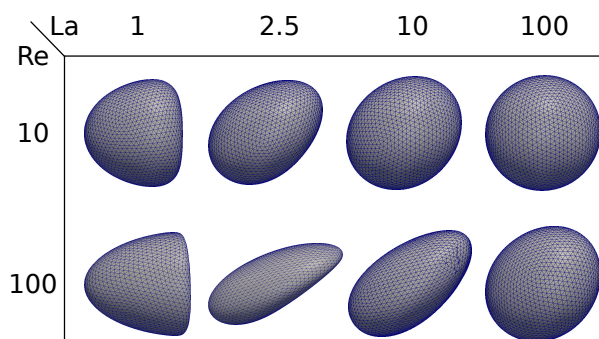


**Fig. 6** Shapes of the capsules for different Laplace and Reynolds numbers.

sules away from the center towards the equilibrium distance of solid spheres. Clearly, since the strength of the inertial forces increases with  $Re$ , the migration towards the channel walls already starts when the capsules are more deformable (large  $Ca$ ).

All curves in the inset roughly have the same shape and shift to the right with increasing  $Re$ . The capillary number  $Ca$  is proportional to the absolute flow velocity  $u_{max}$ . Indeed, removing this dependence and plotting the equilibrium distance versus the Laplace number  $La$ , which measures the rigidity of the capsule, all curves roughly fall onto one master curve [see main plot of Fig. 5a)]. This was already observed by Kilimnik *et al.*<sup>35</sup>. Deviations from the master curve occur for very rigid capsules (large  $La$ ), which move closer to the channel walls with increasing  $Re$ <sup>22,25,59</sup>. Also, the value of  $La$ , where the capsule starts to move away from the channel center, is sensitive to  $Re$ . This might be due to the fact that the shapes of two capsules, located either in the channel center or close-by, differ strongly as we will discuss below.

Also the particle radius  $a/w$  plays an important role for the equilibrium distance, as Fig. 5b) demonstrates. Larger particles leave the channel center at larger  $La$  and thereby assemble closer to the channel center compared to smaller particles. One obvious reason for this behavior is that  $La \propto a$ . However, in addition the lift force, which drives the capsule away from the center, roughly scales with  $a^3$  as discussed in<sup>60</sup> and Sec. 3.3. So, if we plot  $d_{eq}$  versus  $La/(a/w)^4$ , the equilibrium distances collapse on a single master curve in the regime where the capsules are deformable [see inset of Fig. 5b)]. For rigid particles (large  $La$ ) the curves do not collapse since smaller particles move closer to the channel walls<sup>25,34</sup>.

### 3.2 Deformation of the capsules

In Fig. 6 we illustrate the shapes of capsules at their equilibrium positions for different Laplace ( $La$ ) and Reynolds ( $Re$ ) numbers. At  $La = 1$  both capsules are located in the channel center and show the expected form of a parachute, which is more visible at larger Reynolds numbers<sup>61</sup>. At  $La = 2.5$ , the capsules have left the center with  $d_{eq}/w \approx 0.28$  and the deformation is more asymmetric. The capsules become less deformed with increasing  $La$ , although the capsules move further away from the channel center, where the viscous shear stresses increase. Interestingly, although the shapes of capsules with the same  $La$  differ for the two  $Re$  values, in Fig. 5a) we demonstrated that their equilibrium distances to the channel center are roughly the same independent of  $Re$ .

To quantify the deformation of the capsule, we follow<sup>62,63</sup> and determine its moment-of-inertia tensor and then the equivalent ellipsoidal particle with the same principal moments of inertia. Now, the smallest and largest semi-axes of the ellipsoid,  $r_{min}$  and  $r_{max}$ , are then used to define the Taylor deform-



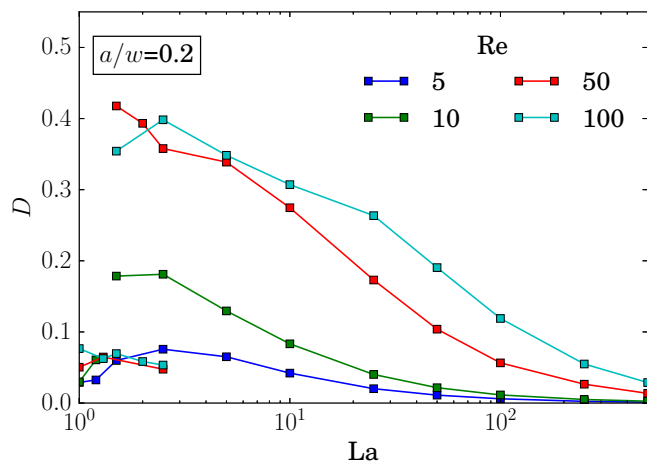


**Fig. 7** Taylor deformation index  $D$  of an elastic capsule at the equilibrium location plotted versus Laplace number  $La$  for different Reynolds numbers  $Re$ .

mation index,

$$D = \frac{r_{\max} - r_{\min}}{r_{\max} + r_{\min}}. \quad (15)$$

For spherical particles it is zero. In Fig. 7 we plot  $D$  versus Laplace number  $La$  for different  $Re$ . The parachute form of soft particles ( $La=1$ ) at the channel center gives a small  $D$ . For  $Re = 5$  when the capsules move away from the center, the deformation index increases smoothly and goes through a maximum, which is approximately situated at  $La \approx 2.5$ . Instead, for  $Re = 10, 50$ , and  $100$  we observe an abrupt increase of  $D$  to another branch. At this point the equilibrium position in the center becomes unstable with increasing  $La$  and sharply increases from zero, as visible in Fig. 6a). However, in our simulations we hardly see the capsules moving away from the center within a simulation time of several million time steps. This is indicated by the extended branches at small  $D$ . For all  $Re$  values we find increasing  $La$  further also reduces  $D$ . For  $Re = 100$  a kink is visible at  $La \approx 25$ . Here the capsule switches its equilibrium location from the diagonal of the channel cross section to one of the main axes.

### 3.3 Lift-force profile

The dynamics and equilibrium positions of an elastic capsule are determined by the lift-force profile. In this section we study how the inertial lift force scales with Reynolds and Laplace number as well as particle radius and compare it to rigid particles. For rigid particles with radii much smaller than the channel width the analytical solution<sup>22,45</sup> for the lift force predicts the scaling  $f_{\text{lift}} \propto Re^2(a/w)^4$ . For larger rigid particles, of similar size as ours, numerical solutions of the Navier-Stokes equations give a scaling proportional to

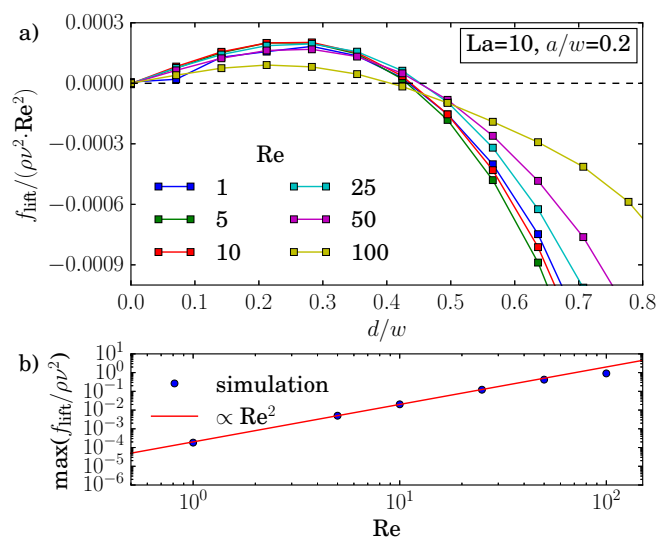


**Fig. 8** a) Inertial lift force  $f_{\text{lift}}$  along the diagonal in units of  $\rho v^2 Re^2$  plotted versus distance  $d/w$  to the center for different Reynolds numbers. Other parameters are  $La = 10$  and  $a/w = 0.2$ . b) Maximum of  $f_{\text{lift}}$  plotted versus  $Re$ .

$Re^2(a/w)^3$  near the channel center and  $Re^2(a/w)^6$  near the channel walls<sup>18</sup>. To measure the lift force we use the procedure described in sect. 2.4. As almost all capsules travel to equilibrium positions on the diagonal, we study the lift-force profiles along this direction.

We usually observe the typical form of the lift-force profile with two equilibrium positions of the capsule, where the lift force vanishes [see, for example, Fig. 8a)]: the unstable fix point in the channel center ( $d = 0$ ) and one stable fix point between channel center and walls. In the previous section we found that the equilibrium position is almost independent of the Reynolds number, in particular, in an intermediate range of capsule rigidity measured by  $La$ . When we measure the lift-force profile for different Reynolds numbers while keeping the particle radius and the Laplace number fixed, this is also visible in the lift-force profiles as all zero crossings coincide [see Fig. 8a)]. Furthermore, the profiles for small  $Re$  fall on top of each other when we scale  $f_{\text{lift}}$  by  $Re^2$ . This scaling is confirmed in Fig. 8b), where we plot the maximum lift force versus  $Re$ . Only for high Reynolds number ( $Re = 100$ ) we obtain a deviation from  $f_{\text{lift}} \propto Re^2$ . Indeed, by measuring the particle-wall interaction of rigid particles, the authors of Ref.<sup>46</sup> noticed an increase of the wall lift coefficient around  $Re \approx 100$  due to an imperfect bifurcation of the wake structure. This might explain our observation. However, in total the scaling law  $f_{\text{lift}} \propto Re^2$  also seems to be valid for soft spheres at moderate  $Re$ .

Figure 9a) confirms the scaling  $f_{\text{lift}} \propto (a/w)^3$  for small distances, while closer to the walls the force profiles clearly

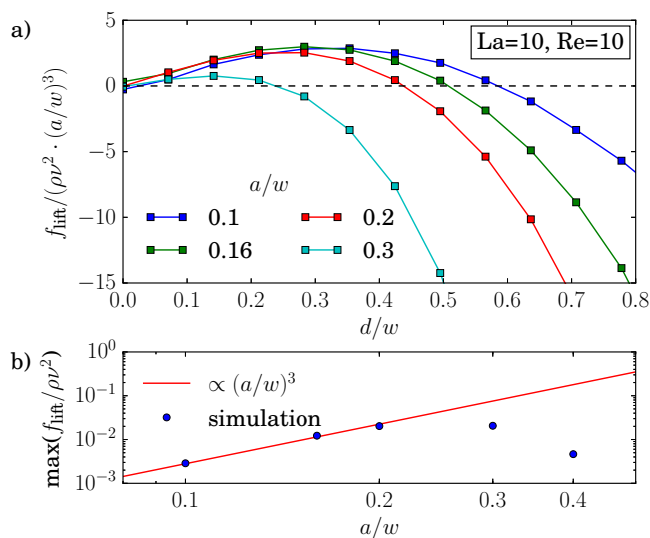


**Fig. 9** a) Inertial lift force  $f_{\text{lift}}$  along the diagonal in units of  $\rho v^2 (a/w)^3$  plotted versus distance  $d/w$  to the center for different particle radii  $a/w$ . Other parameters are  $La = 10$  and  $Re = 10$ . b) Maximum of  $f_{\text{lift}}$  plotted versus  $a/w$ .

differ. Strong deviations also occur for larger particles with  $a/w \geq 0.3$ , which is also visible in the maximum lift force plotted versus  $a/w$  in Fig. 9b). This is in contrast to Refs.<sup>25,60</sup>, where the scaling was verified for particles with radii up to  $a/w = 0.38$ . We suspect the different behavior to be due to the deformability of the capsules.

For increasing Laplace number the lift-force profiles approach the limit of a rigid capsule [see Fig. 10a)]. Making the particles softer, the stable equilibrium position moves towards the channel center and ultimately for  $La = 1$  reaches the center, as already discussed in sect. 3.1. Also, the maximum value of the lift force decreases the softer the particles become as illustrated in Fig. 10b).

### 3.4 External control force

Experiments<sup>39</sup> and simulations<sup>27</sup> showed that the lateral position of rigid particles can be controlled by an external force, applied along the channel axis. Depending on its direction it either speeds up or slows down the particle relative to the channel flow. This changes the relative velocity between particle surface and surrounding fluid. Thereby, the dynamic pressure varies along the surface, which causes the lateral motion of the particle known as Saffman effect<sup>40</sup>. In our simulations we apply a constant force on the elastic capsule evenly distributed on the membrane vertices along the axial direction. We choose the convention that a positive force is directed against the flow and thus slows down the particle. In Fig. 11 we plot the equilibrium distance to the channel center as a

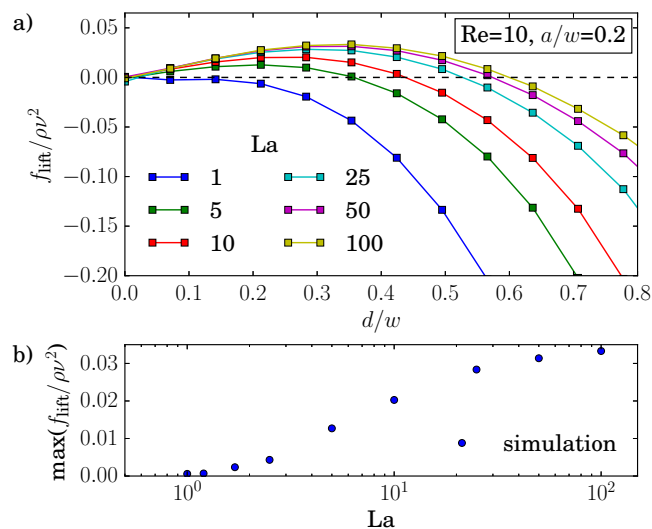


**Fig. 10** a) Inertial lift force  $f_{\text{lift}}$  along the diagonal in units of  $\rho v^2$  plotted versus distance  $d/w$  to the center for different Laplace numbers. Other parameters are  $Re = 10$  and  $a/w = 0.2$ . b) Maximum of  $f_{\text{lift}}$  plotted versus  $La$ .

function of the external control force  $f_{\text{ctrl}}$ . As before, we determined the equilibrium positions from the stable fix points of the lift-force profiles. For rigid capsules ( $La = 500$ ) the results agree with previous simulations<sup>27</sup>: when these particles are slowed down ( $f_{\text{ctrl}} > 0$ ), they move towards the channel center and ultimately reach it for sufficiently large  $f_{\text{ctrl}} > 0$ , while accelerated particles move closer to the channel walls. However, for strongly negative control forces a decrease in the equilibrium distance is observable. This behavior is clearer visible for  $La = 50$ . We observe the softer the capsules are, the more does the maximum equilibrium distance move to larger and even positive control forces. Furthermore, the maximum equilibrium distance decreases until at around  $La \approx 12.5$ , where the curve is symmetric about its maximum. For even softer capsules it increases again. As a consequence, soft particles ( $La = 5$ ) behave opposite to rigid particles: when slowed down, they move away from the channel center, while when moving faster ( $f_{\text{ctrl}} < 0$ ), they approach the center and ultimately stay there.

Even more interesting, we find that all curves for different  $La$  intersect in one point at a positive control force of about  $f_{\text{ctrl}}^* = 1.2\rho v^2$ . At this control force all particles assemble at the same equilibrium distance  $d_{\text{eq}}^*$  independent of their deformability. This property seems to be generic. We also find it for other Reynolds numbers as illustrated in Fig. A2 of appendix A.3. While the intersection point moves to higher control forces with increasing Reynolds number, in fact,  $f_{\text{ctrl}}^* \propto Re$  as Fig. 12 demonstrates, the distance from the channel center stays almost the same at  $\tilde{d}/w \approx 0.46$ . We do not have a clear



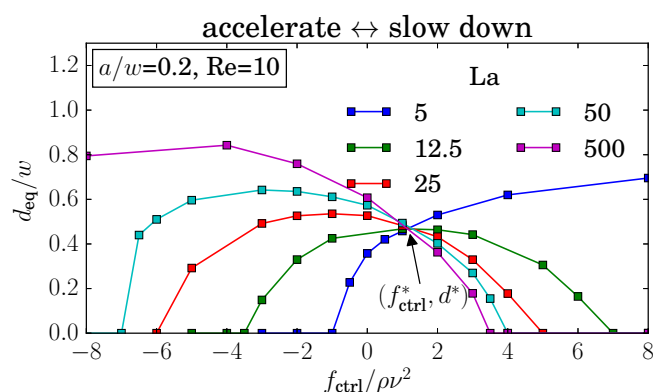


**Fig. 11** Equilibrium distance  $d_{eq}$  plotted versus the external control force  $f_{ctrl}$  for different Laplace numbers  $La$ . Other parameters are  $Re = 10$  and  $a/w = 0.2$ .

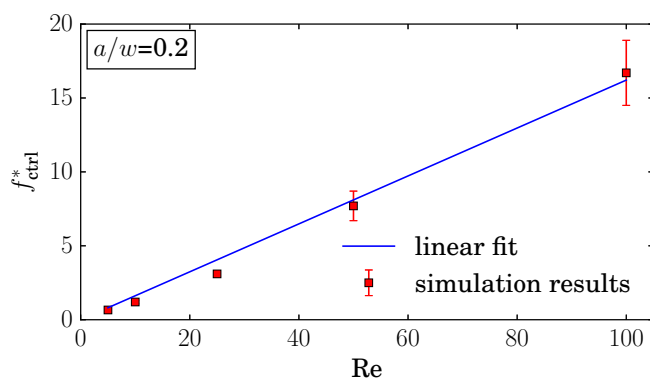


**Fig. 12** Control force of the intersection point  $f_{ctrl}^*$  plotted versus Reynolds number  $Re$ . At lower Reynolds numbers the errorbars are on the order of the symbol size.

understanding of this behavior. However, we checked that it is generic and not a numerical artifact. In particular, this behavior does not change when we increase the channel length to investigate the influence of the periodic boundary condition or when we increase the resolution of the lattice-Boltzmann grid to check for discretization errors (see Fig. A3 in appendix A.3).

Using such an external force, allows a much finer control of the particle's equilibrium position. For example, in the absence of a control force ( $f_{ctrl} = 0$  in Fig. 11) the equilibrium position of particles with  $La = 5$  and  $La = 12.5$  are quite close to each other. By applying  $f_{ctrl} = -1\rho v^2$  the softer particle moves towards the center while the equilibrium position of the less deformable particle hardly changes. This effect should help to enhance particle separation based on its deformability.

## 4 Conclusions

Manipulating deformable capsules by hydrodynamic flow in the regime of intermediate Reynolds numbers has a large variety of applications, e.g., for cell sorting or probing. The high fluid velocities allow a high throughput and the resulting inertial focusing can be used to separate and steer particles towards desired positions within a channel. In this work we studied the equilibrium positions of soft capsules while immersed in a Poiseuille flow through a quadratic channel. We find that most particles assemble along the diagonal of the channel. The softer the particles are the closer they move towards the channel center. Their final equilibrium distance depends on the particle deformability, its radius and the channel Reynolds number. By introducing the Laplace number as ratio of elastic force to the intrinsic viscous force scale, the equilibrium position for different Reynolds numbers collapse on a single master curve. The equilibrium distance is thus independent of the flow velocity. Additionally, we also identify such a date collapse for different particle radii.

In contrast to the equilibrium distance we find that the deformation of the capsules strongly depends on the Reynolds number. The deformation of the off-centered capsules increases with decreasing Laplace number although the capsules migrate in areas with a smaller shear gradient. Very soft capsules assemble at the channel center and have a symmetric parachute shape.

The lift-force profiles of deformable capsules behave pretty much the same as those of rigid particles, where the lift force scales as  $f_{lift} \propto Re^2(a/w)^3$ . For deformable capsules, we find deviations from this scaling law only for high Reynolds number ( $Re = 100$ ) and large particles ( $a/w = 0.3$ ). We were not able to identify a similar scaling involving the Laplace number. For decreasing  $La$ , the stable equilibrium position moves towards the channel center and the maximum value of the lift force decreases until only a stable fixpoint in the channel center remains.

Finally, we demonstrated that the particle equilibrium position can be controlled by an external force along the channel axis. For almost rigid particles ( $La = 500$ ) we confirmed previous results<sup>27</sup>, but found a new behavior for soft particles. While rigid particles migrate towards the channel center when they are slowed down, moderately soft particles with  $La \approx 12.5$  migrate towards the channel center both for positive and negative control forces. For even lower  $La$  the capsules behave opposite to rigid particles as they move towards the channel wall when slowed down. Interestingly, we observe that all graphs with different Laplace numbers intersect in one point at a non-zero control force.

Cancer cells are softer than healthy cells<sup>2</sup>. Using an external control force, enhances the sensitivity to separate them based on the lateral locations they assume in microchannels.

Thus, our new theoretical insights might prove useful in developing new biomedical devices to probe and separate cells based on their size and deformability.

## 5 Acknowledgments

We thank C. Prohm for providing the source code and for initial work in the project. We acknowledge support from the Deutsche Forschungsgemeinschaft in the framework of the Collaborative Research Center SFB 910.

## References

- G. Y. H. Lee and C. T. Lim, *Trends in Biotechnology*, 2007, **25**, 111–118.
- S. Suresh, *Acta Biomater*, 2007, **3**, 413–438.
- J. Guck, S. Schinkinger, B. Lincoln, F. Wottawah, S. Ebert, M. Romeyke, D. Lenz, H. M. Erickson, R. Ananthakrishnan, D. Mitchell, J. Käs, S. Ulvick and C. Bilby, *Biophys. J.*, 2005, **88**, 3689–3698.
- H. A. Cranston, C. W. Boylan, G. L. Carroll, S. P. Suter, Williamson, I. Y. Gluzman and D. J. Krogstad, *Science*, 1984, **223**, 400–403.
- S. Suresh, J. Spatz, J. P. Mills, A. Micoulet, M. Dao, C. T. Lim, M. Beil and T. Seufferlein, *Acta Biomaterialia*, 2005, **1**, 15–30.
- O. Otto, P. Rosendahl, A. Mietke, S. Golfier, C. Herold, D. Klaue, S. Giarardo, S. Pagliara, A. Ekpenyong, A. Jacobi, M. Wobus, N. Töpfner, U. F. Keyser, J. Mansfeld, E. Fischer-Friedrich and J. Guck, *Nat. Methods*, 2015, **12**, 199–202.
- H. W. Hou, A. A. S. Bhagat, A. G. Lin Chong, P. Mao, K. S. Wei Tan, J. Han and C. T. Lim, *Lab. Chip*, 2010, **10**, 2605.
- L. R. Huang, E. C. Cox, R. H. Austin and J. C. Sturm, *Science*, 2004, **304**, 987–990.
- T. M. Geislinger, B. Eggart, S. Braunmüller, L. Schmid and T. Franke, *Appl. Phys. Lett.*, 2012, **100**, 183701.
- D. Bell, C. Wongsrichanalai and J. W. Barnwell, *Nat. Rev. Microbiol.*, 2006, **4**, S7–S20.
- G. Couplier, B. Kaoui, T. Podgorski and C. Misbah, *Phys. Fluids*, 2008, **20**, 111702.
- F. Risso, F. Collé-Paillot and M. Zagzoule, *J. Fluid Mech.*, 2006, **547**, 149–173.
- P. Bagchi, *Biophysical Journal*, 2007, **92**, 1858–1877.
- G. R. Lázaro, A. Hernández-Machado and I. Pagonabarraga, *Soft Matter*, 2014, **10**, 7207–7217.
- C. Bächer, L. Schrack and S. Gekle, *Phys. Rev. Fluids*, 2017, **2**, year.
- B. Kaoui, G. H. Ristow, I. Cantat, C. Misbah and W. Zimmermann, *Phys. Rev. E*, 2008, **77**, 021903.
- G. Segré and A. Silberberg, *Nature*, 1961, **189**, 209–210.
- D. Di Carlo, *Lab. Chip*, 2009, **9**, 3038.
- J. P. Matas, J. F. Morris and E. Guazzelli, *Oil Gas Sci. Technol.*, 2004, **59**, 59–70.
- D. D. Carlo, D. Irimia, R. G. Tompkins and M. Toner, *PNAS*, 2007, **104**, 18892–18897.
- A. A. S. Bhagat, S. S. Kuntaegowdanahalli and I. Papautsky, *Microfluid. Nanofluidics*, 2009, **7**, 217–226.
- E. S. Asmolov, *J. Fluid Mech.*, 1999, **381**, 63–87.
- J. A. Schonberg and E. J. Hinch, *J. Fluid Mech.*, 1989, **203**, 517–524.
- B. Chun and A. J. C. Ladd, *Phys. Fluids*, 2006, **18**, 031704.
- C. Prohm, M. Gierlak and H. Stark, *Eur. Phys. J. E*, 2012, **35**, year.
- W. Lee, H. Amini, H. A. Stone and D. Di Carlo, *Proc. Natl. Acad. Sci.*, 2010, **107**, 22413–22418.
- C. Prohm and H. Stark, *Lab. Chip*, 2014, **14**, 2115.
- D. Salac and M. J. Miksis, *J. Fluid Mech.*, 2012, **711**, 122–146.
- A. J. Mach and D. Di Carlo, *Biotechnol. Bioeng.*, 2010, **107**, 302–311.
- S. K. Doddhi and P. Bagchi, *Int. J. Multiph. Flow*, 2008, **34**, 966–986.
- D.-K. Sun and Z. Bo, *Int. J. Heat Mass Transf.*, 2015, **80**, 139–149.
- B. Kim, C. B. Chang, S. G. Park and H. J. Sung, *Int. J. Heat Fluid Flow*, 2015, **54**, 87–96.
- Z. Wang, Y. Sui, A.-V. Salsac, D. Barthès-Biesel and W. Wang, *J. Fluid Mech.*, 2016, **806**, 603–626.
- S. C. Hur, N. K. Henderson-MacLennan, E. R. B. McCabe and D. Di Carlo, *Lab. Chip*, 2011, **11**, 912.
- A. Kilimnik, W. Mao and A. Alexeev, *Phys. Fluids*, 2011, **23**, 123302.
- Y.-L. Chen, *RSC Adv*, 2014, **4**, 17908–17916.
- T. Krüger, B. Kaoui and J. Harting, *J. Fluid Mech.*, 2014, **751**, 725–745.
- S. J. Shin and H. J. Sung, *Phys. Rev. E*, 2011, **83**, year.
- Y. W. Kim and J. Y. Yoo, *Lab. Chip*, 2009, **9**, 1043.
- P. G. T. Saffman, *J. Fluid Mech.*, 1965, **22**, 385–400.
- C. Prohm, N. Zöller and H. Stark, *Eur. Phys. J. E*, 2014, **37**, year.
- C. Prohm, F. Tröltzsch and H. Stark, *Eur. Phys. J. E*, 2013, **36**, year.
- H. Bruus, *Theoretical Microfluidics*, Oxford University Press, Oxford ; New York, 2008.
- R. Fåhræus, *Physiol. Rev.*, 1929, **9**, 241–274.
- G. Segré and A. Silberberg, *J. Fluid Mech.*, 1962, **14**, 136–157.
- L. Zeng, S. Balachandar and P. Fischer, *J. Fluid Mech.*, 2005, **536**, 1–25.
- S. Succi, *The Lattice Boltzmann Equation for Fluid Dynamics and Beyond*, Clarendon Press ; Oxford University Press, Oxford : New York, 2001.
- P. L. Bhatnagar, E. P. Gross and M. Krook, *Phys. Rev.*, 1954, **94**, 511–525.
- B. Dünweg and A. J. Ladd, in *Advances in Polymer Science*, Springer Berlin Heidelberg, 2008, pp. 1–78.
- Z. Guo, C. Zheng and B. Shi, *Phys. Rev. E*, 2002, **65**, year.
- The Palabos Project*, 2013, <http://www.palabos.org/>.
- C. S. Peskin, *Ph.D. thesis*, PhD thesis, Albert Einstein College of Medicine, 1972.
- C. S. Peskin, *Acta Numer.*, 2002, **11**, 479–517.
- T. Krüger, F. Varnik and D. Raabe, *Comput. Math. Appl.*, 2011, **61**, 3485–3505.
- R. Skalak, A. Tozeren, R. P. Zarda and S. Chien, *Biophys. J.*, 1973, **13**, 245.
- W. Helfrich, *Z Naturforsch C*, 1973 Nov-Dec, **28**, 693–703.
- G. Gompper and D. M. Kroll, *J. Phys. I France*, 1996, **6**, 1305–1320.
- K. J. Åström and R. M. Murray, *Feedback Systems: An Introduction for Scientists and Engineers*, Princeton University Press, Princeton, 2008.
- J.-P. Matas, J. F. Morris and É. Guazzelli, *J. Fluid Mech.*, 2004, **515**, 171–195.
- D. Di Carlo, J. F. Edd, K. J. Humphry, H. A. Stone and M. Toner, *Phys. Rev. Lett.*, 2009, **102**, year.
- J. Horwitz, P. Kumar and S. Vanka, *Int. J. Multiph. Flow*, 2014, **67**, 10–24.
- G. I. Taylor, *Proc. R. Soc. Lond. Math. Phys. Eng. Sci.*, 1934, **146**, 501–523.
- S. Ramanujan and C. Pozrikidis, *J. Fluid Mech.*, 1998, **361**, 117–143.

## A Appendices

### A.1 Determining the equilibrium distance

To determine the equilibrium distance of the elastic capsule from the channel center, we considered two different methods as described in sect. 3.1.

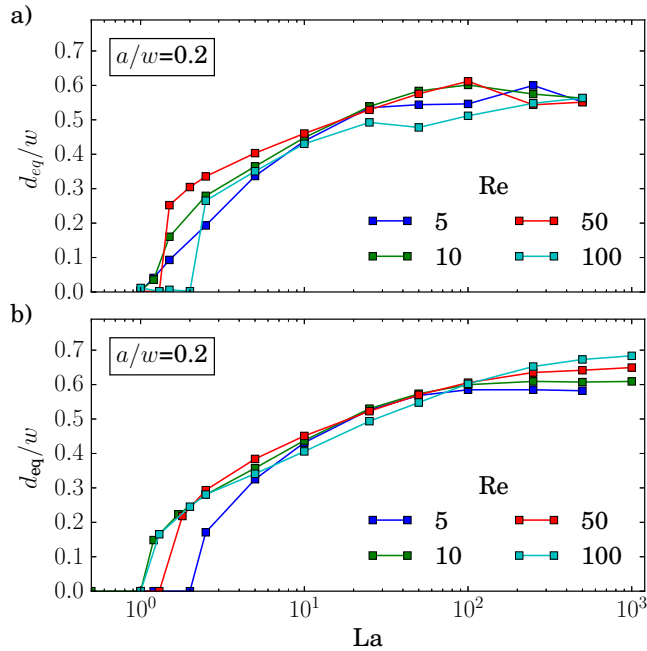


**Fig. A1** Equilibrium distance from the center as a function of the Laplace number determined by two different methods. a) Particles are placed in the flow and migrate freely to their equilibrium position; b) the equilibrium distance is extracted from the stable fix points of the lift-force profiles. Both plots agree quite well.

### A.2 Green strain tensor

Skalak *et al.*<sup>55</sup> introduced a model for the strain energy of the membrane of a red blood cell. It is formulated in the framework of finite strain theory, which investigates the deformation of a body relative to a reference configuration. We denote the reference coordinates by  $\vec{x}$  and the coordinates of the deformed state by  $\vec{y}$ . In the coordinate system, where the local Jacobi matrix  $\partial y_i / \partial x_j$  is diagonal, the extension ratios  $\lambda_1$  and  $\lambda_2$  are given by

$$\lambda_1 = \frac{\partial y_1}{\partial x_1} \quad \text{and} \quad \lambda_2 = \frac{\partial y_2}{\partial x_2}. \quad (\text{A1})$$

Now, deformations can be described by the Green strain tensor, the components of which are defined as

$$e_{11} = \frac{1}{2} (\lambda_1^2 - 1) \quad \text{and} \quad e_{22} = \frac{1}{2} (\lambda_2^2 - 1). \quad (\text{A2})$$

Furthermore, the authors introduced the strain energy function  $E_s$  of Eq. (7) to calculate the Piola-Kirchoff stress tensor

$$S_{ij} = \frac{\partial E_s}{\partial e_{ij}} \quad (\text{A3})$$

where  $S_{ij}$  is the tension in the membrane in terms of the reference coordinates  $\vec{x}$ . The Piola-Kirchoff stress tensor is related to the Cauchy stress tensor by

$$\sigma = \frac{1}{\lambda_1 \lambda_2} S_{kl} \frac{\partial y_i}{\partial x_k} \frac{\partial y_j}{\partial x_l} \quad (\text{A4})$$

The strain energy is a scalar function and invariant under all local rotations of the two-dimensional membrane about the normal. Thus, it can only depend on the invariants of the Green strain tensor, which are written as

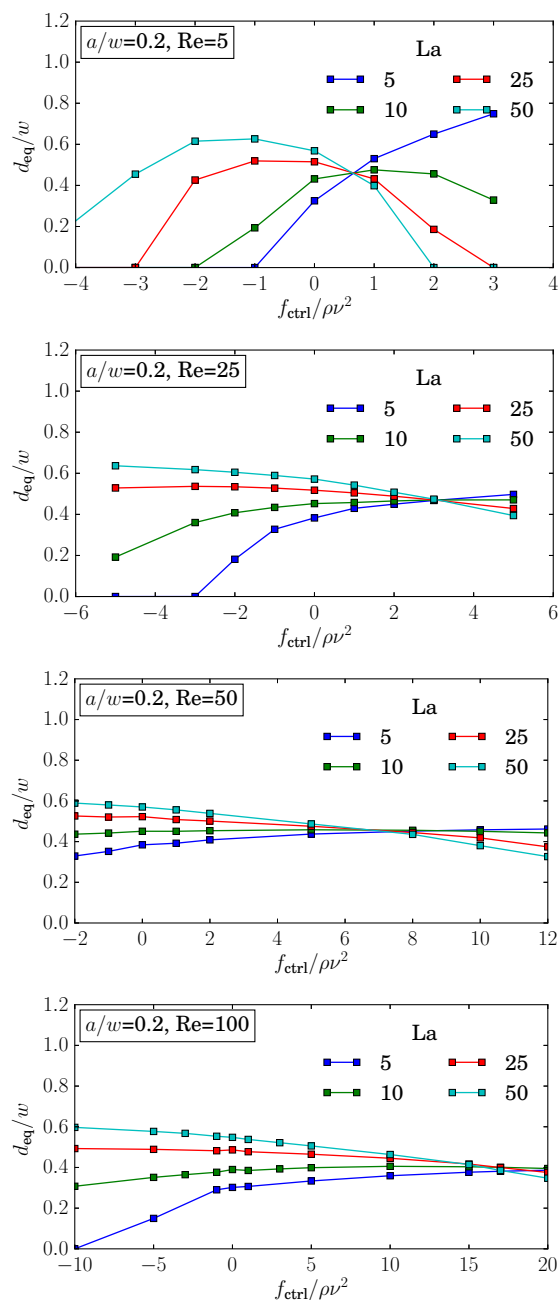
$$I_1 = 2(e_{11} + e_{22}) = \lambda_1^2 + \lambda_2^2 - 2 \quad (\text{A5})$$

$$I_2 = 4e_{11}e_{22} + I_1 = \lambda_1^2 \lambda_2^2 - 1. \quad (\text{A6})$$

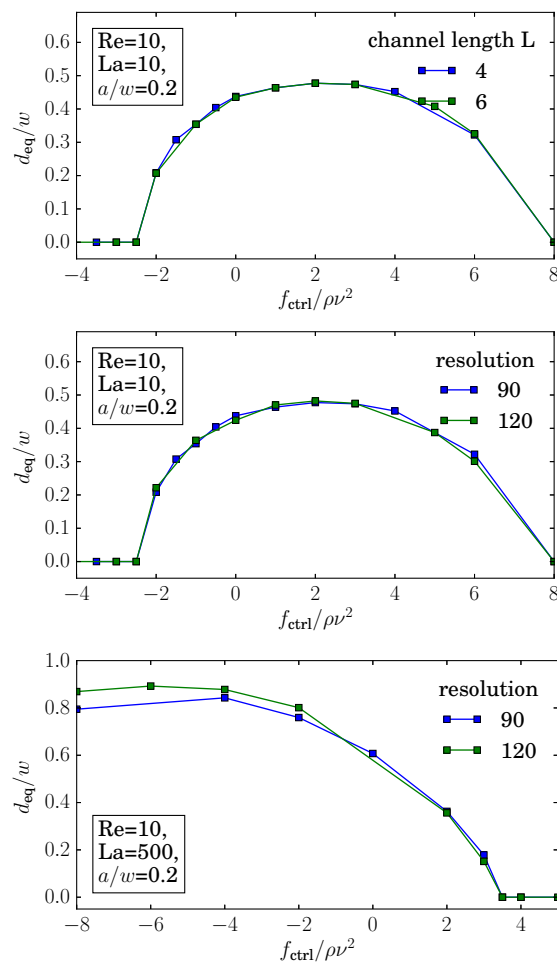
### A.3 Equilibrium distance for external control force

Figure A2 shows the equilibrium distance plotted versus the control force for different Laplace numbers and Reynolds numbers. The curves for different  $La$  intersect in one point. This is valid for all Reynolds numbers. With increasing  $Re$  the intersection point moves towards higher forces while the equilibrium distance only varies little.

As demonstrated in Fig. A3, the graphs for the equilibrium distance plotted versus control force is independent of the channel length  $L$ , the resolution of the lattice-Boltzmann grid. Only for rigid particles ( $La = 500$ ), one observes small deviations, when the particles are located close to the walls.



**Fig. A2** The equilibrium distance  $d_{eq}$  plotted versus control force  $f_{ctrl}$  for different Laplace numbers  $La$  and Reynolds numbers  $Re = 5, 25, 50, 100$  for particle radius  $a = 0.2w$ .



**Fig. A3** The equilibrium distance  $d_{eq}$  plotted versus control force for different channel lengths (top) and different resolutions of the lattice-Boltzmann grid for  $La = 10$  (middle) and  $La = 500$  (bottom).